STUDY ON FAILURE MECHANISMS OF RAINFALL-INDUCED LANDSLIDES USING PHYSICAL MODEL EXPERIMENT AND NUMERICAL ANALYSIS

Thanh Son Nguyen[a,*], Trong-Toan Phan[b], Cong-Son Ha[b], Ba-Danh Le[a]

*[a]Faculty of Bridges and Roads, Hanoi University of Civil Engineering,
55 Giai Phong road, Hai Ba Trung district, Hanoi, Vietnam
[b]Faculty of Building and Industrial Construction, Hanoi University of Civil Engineering,
55 Giai Phong road, Hai Ba Trung district, Hanoi, Vietnam*

Abstract

Landslides are one of the most prevalent geological disasters in nature and rainfall infiltration is one of the key triggering factors of landslides. In this study, a laboratory flume model experiment was performed to investigate rainfall infiltration processes and failure mechanisms of sand slopes under artificial rainfall of 90 mm/h. The numerical simulation was then performed to compare the hydraulic responses and failure mechanism of the slope observed in the experiment. The results of the physical slope model demonstrated that water impounding and a sudden increase in water level at the slope foot causes the local failure near the slope toe, followed by the development of cracking and retrogressive sliding extending up to the slope's crest. The simulated results of the phreatic level are in good agreement with the experimental results, indicating the numerical proposed is capable of quantitatively well the hydraulic responses of slope upon rainfall. Both physical and numerical model results highlighted a positive correlation between slope failure and the development of the phreatic level within the slope. The results of this study would provide insights into the slope failure process and provide a dependable methodology for devising solutions to reduce the risk of landslides induced by rainfall infiltration.

Keywords: physical model test; rainfall-induced landslide; moisture content; porewater pressure; infiltration; deep-seated landslides.

1. Introduction

Landslides are frequent natural disasters, particularly in mountainous regions worldwide, leading to substantial damage to infrastructure and significant economic losses [1, 2]. According to a global database reported by Froude and Petley [3], during the period (2004–2016), approximately 55997 fatalities resulted from 4862 distinct landslide events, with projections indicating an increase in such occurrences due to climate change. Over the past decade alone, natural disasters in Vietnam have caused significant devastation, resulting in over 9500 casualties and annual economic losses estimated at 1.5–1.8% of GDP. Among various triggering factors, such as topographic features, weathering processes, earthquakes, and human activities, rainfall infiltration has been identified as a primary natural contributor to landslide formation [4, 5]. Data from the National Group for Prevention of Hydrological Hazards in Italy (CNR-GNDCI, http://avi.gndci.cnr.it) reveal that rainfall precipitation accounts for 73.5% of landslide occurrences, followed by erosion (11.9%), anthropic activity (5.1%), earthquakes (2.6%), and groundwater variation (1.4%). In Taiwan, the statistical data compiled from 270 natural disaster events over 50 years (1958-2007) [6] indicate that 71.1% of failures were attributed

---

Corresponding author. E-mail address: sonnt@huce.edu.vn (Nguyen, T. S.)

to typhoons, 15% to flooding, earthquakes (8.5%), torrential rainfall (2.2%), wind-storms (1.5%), mountain flooding (0.7%), and landslides (0.7%). In particular, their statistical data revealed that 89% of landslide incidents were associated with heavy rainfall.

The study of hydraulic responses and failure mechanisms of slopes under rainfall infiltration is crucial for effectively predicting the occurrence of rainfall-induced landslides. Currently, there are four main approaches to explore the mechanism of rainfall-induced slope failures, including small-scale experiments using flume tests [7–11]; field observations [12]; numerical analyses [13–15], and theoretical models [16–18]. The findings from these studies indicate that for shallow landslide events (i.e., when the critical slip surface depth ranges between 0.5 m and 5 m), rainwater infiltrations leads to an increase in porewater pressure (PWP) in the soil, resulting in a reduction in matric suction and decreased shear strength of the soil, ultimately leading to slope instability [7, 19]. Meanwhile, for deep-seated landslide events (where the critical slip surface depth exceeds 5 m), most of the deep-seated landslide failures are attributed to the rise of the groundwater table along a distinct slip surface.

Among the aforementioned approaches, experimental tests using physical models remain the most reliable method for gaining deep insight into the failure process, mode, and mechanisms of slope failure due to rainfall. A notable advantage of physical modeling is its ability to separately analyze the role of various factors (such as soil properties, slope geometry, and rainfall intensity) on slope behavior up to failure in a controlled environment and under predefined boundary conditions [20]. Wang and Sassa [21] performed a series of tests on fine silty sands to study the mechanism of flowslides under conditions of rainfall and the effects of finer grains, initial void ratio on flowslide motion. Their model test results revealed that grain size and fine-particle contents can have a significant impact on the mobility of rainfall-induced shallow landslides. Tohari et al. [22] carried out experimental tests using physical slope models to investigate the slope failure mechanism. They observed that the slope failure was initiated when the moisture content at the toe reached saturation. Schnellmann et al. [23] developed physical slope models to study the effect of rising groundwater table on porewater pressures and water content of slope upon rainfall. Regmi et al. [24] conducted flume experiments to investigate the failure process of slope due to rainfall events, in which they observed that the slope failure initiating once at the region near the toe results in successive sliding failures. Chueasamat et al. [25] conducted a series of experimental tests using reduced-scale (i.e., 1g) slope models with different combinations of rainfall intensities and relative sand densities. Two types of failures namely surface slide failure and retrogressive failure were observed through experiments. Surface slide failure occurred when the small relative density soil or high rainfall intensity was adopted, whereas the retrogressive failure occurred when the high relative density and low rainfall intensity was used in the tests. Cogan and Gratchev [9] performed a series of flume experiments to investigate slope characteristics on landslide initiation under different initial moisture content, slope angle, and rainfall intensity. Through the physical modeling, the characteristics of the failure mechanism, the responses of moisture content, the PWP distribution, stress, and shear deformation along the sliding zone of the flowslides were observed and clarified. Despite numerous previous efforts to explore the mechanisms of slope failure due to rainfall, there remains a notable gap in the literature regarding the role of rainwater in triggering deep-seated landslides.

The aim of this study is to investigate and understand the development of positive PWP in relation to deep-seated slope initiation through the use of a flume experiment. A finite element numerical model utilizing Geo-Studio SEEP/W software [26] was then employed to validate the hydraulic processes contributing to slope failure observed during rainfall in the experiment. The findings obtained from this study can significantly enhance the understanding of the formation mechanism of deep-

seated landslides under rainfall infiltration, and they serve as a basis for proposing remedial measures in the future.

2. Experimental program

2.1. Equipment and flume detail

In order to study the mechanism of rainwater in triggering deep-seated landslides small-scale test was conducted to replicate the mechanical response of a field prototype structure The experiment flume (Fig. 1) has a dimension of 200 mm (long) × 600 mm (wide) × 700 mm (high). The framework was made of stainless steel, and the base was a flat steel plate of 15 mm. The model slope consists of a 0.45-m-deep sand. This depth also allows for a comprehensive examination of the entire process leading to slope failures, as well as enables detailed monitoring of porewater pressure evolution The slope gradient of the upper part flume was 20°. The sidewalls of the flume were made of transparent tempered glass, enabling the direct observation of the deformation and processes of slope collapse The lower end of the flume is open, allowing free discharge of water to the outside. Additionally, many drainage holes were installed at the lower part of the model to allow excess water to drain whilst still enabling full infiltration within the slope. The inner surface of the flume was carefully treated using lubricating oil to minimize the side friction at the soil- sidewall interface. Additionally, to minimize water infiltration between the sidewalls of the flume and the adjacent soil, transparent plastic sheets were used to seal the boundaries. Two digital photo cameras with a resolution of 1920×1080 pixels placed in the sides and one was placed in the front of the flume test to retrieve the displacement and monitor the failure mechanism. The failure process of the experimental model was evaluated and determined through video footage, camera photography and visual observation with the eyes. Fig. 1 displays the flume dimensions and artificial rainfall simulator.
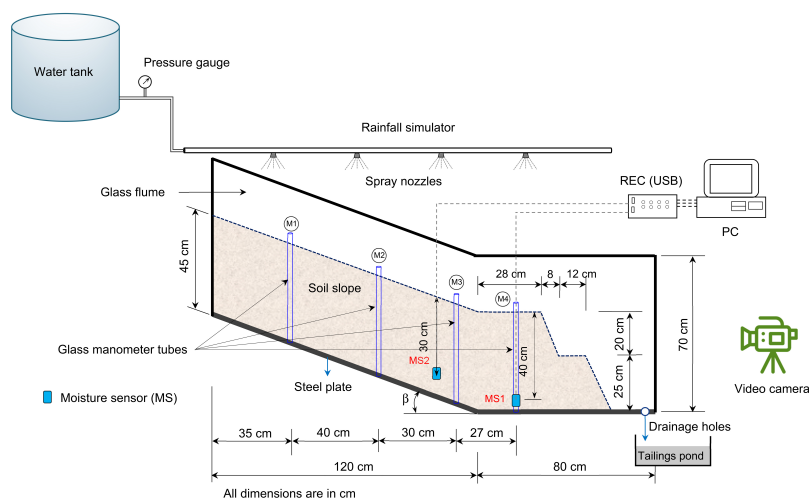

Figure 1. Concept of flume experiment, artificial rainfall, locations of soil moisture (MS1, MS2), and glass manometer tubes (M1, M2, M3, M4)

Two soil moisture sensors (i.e., MS1 and MS2) were installed to record the changes in the soil moisture content over time during rainfall. MS1 and MS2 sensors were installed at 50 mm and 150 mm from the base of soil, respectively (Fig. 1). The soil moisture sensor has three probes, with a length of 70 mm and a spacing of 15 mm (Fig. 2(a)) and its measuring range was from 0% to 100% and the measurement accuracy device is ±3%. Besides, to measure the hydraulic responses (i.e., development of water level) during water infiltration, four glass manometer tubes (diameter = 16 mm) (Fig. 2(b))

were installed vertically along of the slope during the construction. The location of the sensors and manometer tubes used in the experimental test are shown in Fig. 1. Fig. 2 shows the soil moisture sensors and glass manometer tubes detail.
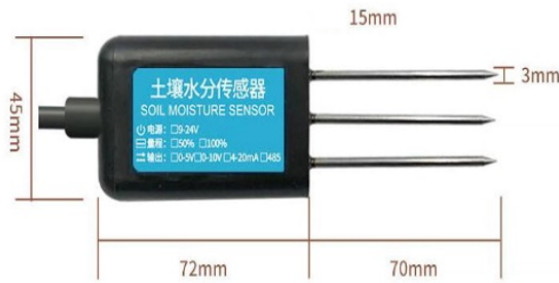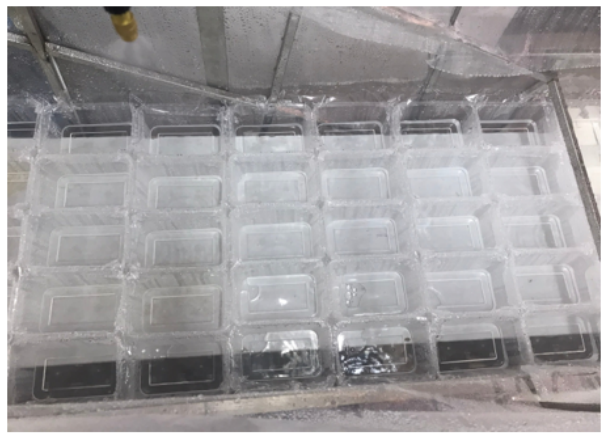

(a) Moisture sensor (RS485)
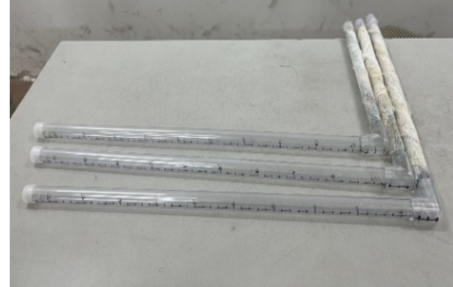
(b) Glass manometer tubes

(c) Spray nozzles

(d) Transparent boxes to determine the uniformity of the applied rainfall

Figure 2. Pictures of the measuring system used in model test

2.2. Rainfall simulation system

Rainfall intensity is a key parameter in the study of rainfall simulator and it depends on the type of the spray nozzle selected for the experiment [27]. In this experimental test, the artificial rainfall system is mounted on top of the box, which consisted of a water tank, a pressure regulator valve, spray nozzles, steel frame as well as pipeline. First, water is supplied from a water tank connected to the water supply system. After that, it is pumped up through a main water pipe divided into two pipe rows, each row has four nozzles A total of eight spray nozzles were used in this test to ensure the uniform distribution of rainfall on the flume (Fig. 3). The water particles had a diameter of about 0.1 mm in order to avoid erosion of the ground surface. The distance between the nozzles was set at 340 mm for rainfall intensities design of 90 mm/h. Because the pressure at the nozzle affects the rainfall intensity, a fixed water supply pressure at 170 kPa was controlled at the water supply head through a pressure regulator valve. It is notable that the rainfall intensities were chosen in this experimental test based on soil infiltration characteristics (k_s) and existing rainfall simulator equipment capabilities, with the main requirement being that all water over the soil model surface infiltrate without causing surface runoff.
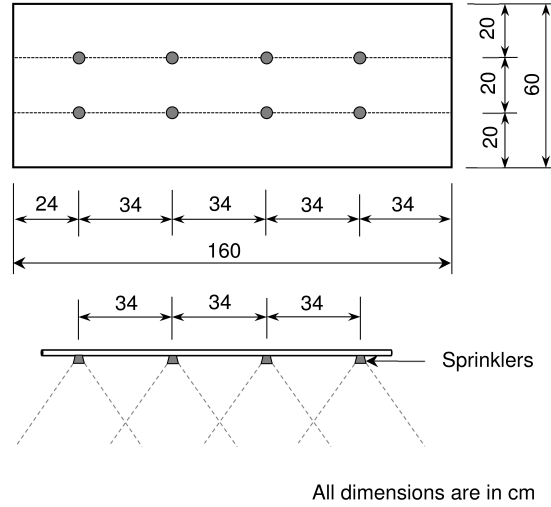
All dimensions are in cm

Figure 3. Nozzle scheme on the oscillating bar for rainfall intensities of 90 mm/h

To evaluate the sprinkle uniformity of the artificial rainfall distributed over the slope surface, forty nine transparents boxes (Fig. 2(d)) were placed inside the flume test to collect the applied rainwater. Rainfall was applied at different times (i.e., 3-, 6-, and 9- minute). Subsequently, all boxes were weighed (or volume) and the rainfall intensity was calculated. According to Christiansen [28], the uniform distribution of rainfall is evaluated through the Christiansen Uniformity Coefficient (CuC), which is defined as follows:

$$CuC = \left[1 - \frac{\sum\limits_{i=1}^{n} |x_i - \bar{x}|}{\sum\limits_{i=1}^{n} x_i} \right] \times 100 \tag{1}$$

where *CuC* is the Christiansen's uniformity coefficient (%), x_i is the rainwater collected in the i-th box, and $\bar{x}$ is the average rainwater value from all the boxes, n is the number of collecting box. A rainfall can be considered uniform when *CuC* is higher than 80% as recommended by Aksoy et al. [29]. The test results indicated the irrigation system used in this study achieved *CuC* = 88.4%, suggesting the irrigation system produced simulated rainfall with a reasonably high uniformity.

2.3. Soil material properties

Experiments used one soil type as a coarse-grained sand with a coefficient of uniformity of C_u = 3.64, a coefficient of curvature of C_c = 1.15, a specific gravity (G_s) of 2.66. The maximum and minimum dry unit weights of the sand were $\gamma_{d,max}$ = 16.78 kN/m³ and $\gamma_{d,min}$ = 15.84 kN/m³, respectively. Fig. 4 shows the grain size distribution curve of sand.

Direct shear tests were performed in accordance with TCVN 4199-1995 standard. Shear box tests were performed on specimens with different percentages of moisture contents of 13%, 15%, 25%, and 30%. Fig. 4 plots the Mohr–Coulomb failure envelopes The shear strength test result (Fig. 5) showed that the internal friction angle and soil apparent cohesion were 325° and 11 kN/m², respectively under total stress at a water content of 15% The hydraulic conductivity (k_s) of saturated soil specimens based on a standard constant head test was 2.5×10^4 m/s. In this experimental test, each 15 cm-thick soil layer was compacted by 10 passings of a steel roller to the relative density, D_r about 55%. A total of three layers of soil were compacted independently and piled up in sequence at the same initial soil moisture content and relative density to ensure homogeneous conditions. The physical and
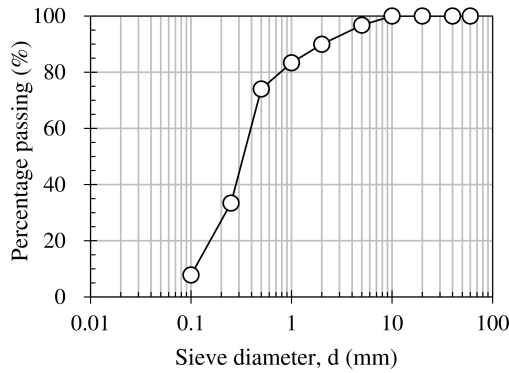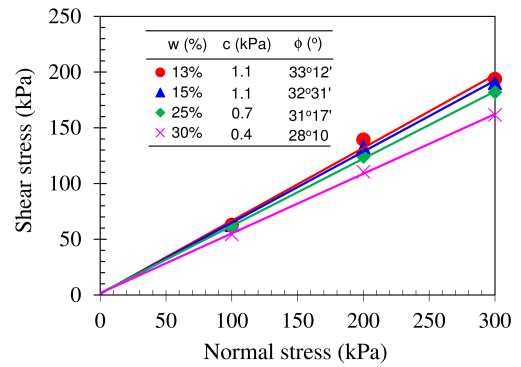
Figure 4. Grain size distribution curves

Figure 5. Mohr–Coulomb failure envelopes under different water content conditions

mechanical parameters of soils summarized in Table 1. The targeted initial soil moisture at the start of the experimental model construction was designed 13.3% in this study, which is close to the optimum moisture content. During construction, the initial water content was determined for each batch of soil and the amount of water needed to be added will be carefully calculated to achieve the required moisture level.

Table 1. Soil properties in a flume experiment

Parameters	Value
Particle density, (g/cm^3)	2.66
Uniformity coefficient, C_u	3.64
Curvature coefficient, C_c	1.15
Initial water content, %	4
Optimum water content, %	13.25
Maximum dry unit weight, (kN/m^3)	16.78
Minimum dry unit weight, (kN/m^3)	15.84
Soil classification (as TCVN 9362:2012)	Medium coarse sand (SP)
Hydraulic conductivity, k_s (m/s)	2.5×10^{-4}

(a) Front view

(b) Side view

Figure 6. Photo of the physical slope model

3. Experimental results

After installing the soil material and monitoring equipment within the slope model, the slope model test were exposed to artificial rainfall from rainfall simulator system. A artificial rainfall simulation of 90 mm/h was carried out continuously from 16:05 pm to 17:00 pm (until the landslide was completed) with a cumulative rainfall duration of about one hour. For the later convenience of descriptions, elapsed time t denotes the time that passed from the start of the rainfall process. For example, the starting time of the rainfall was 16:05 pm and is expressed as 0 h, t_p is the time to occur initial failure, t_{cr} is the time when the first crack was observed on the slope surface, t_f is the time when an obvious landslide movement happen.

| (a) $t = 0$ h | (b) $t = 2230$ sec | (c) $t = 2320$ sec | (d) $t = 2325$ sec |

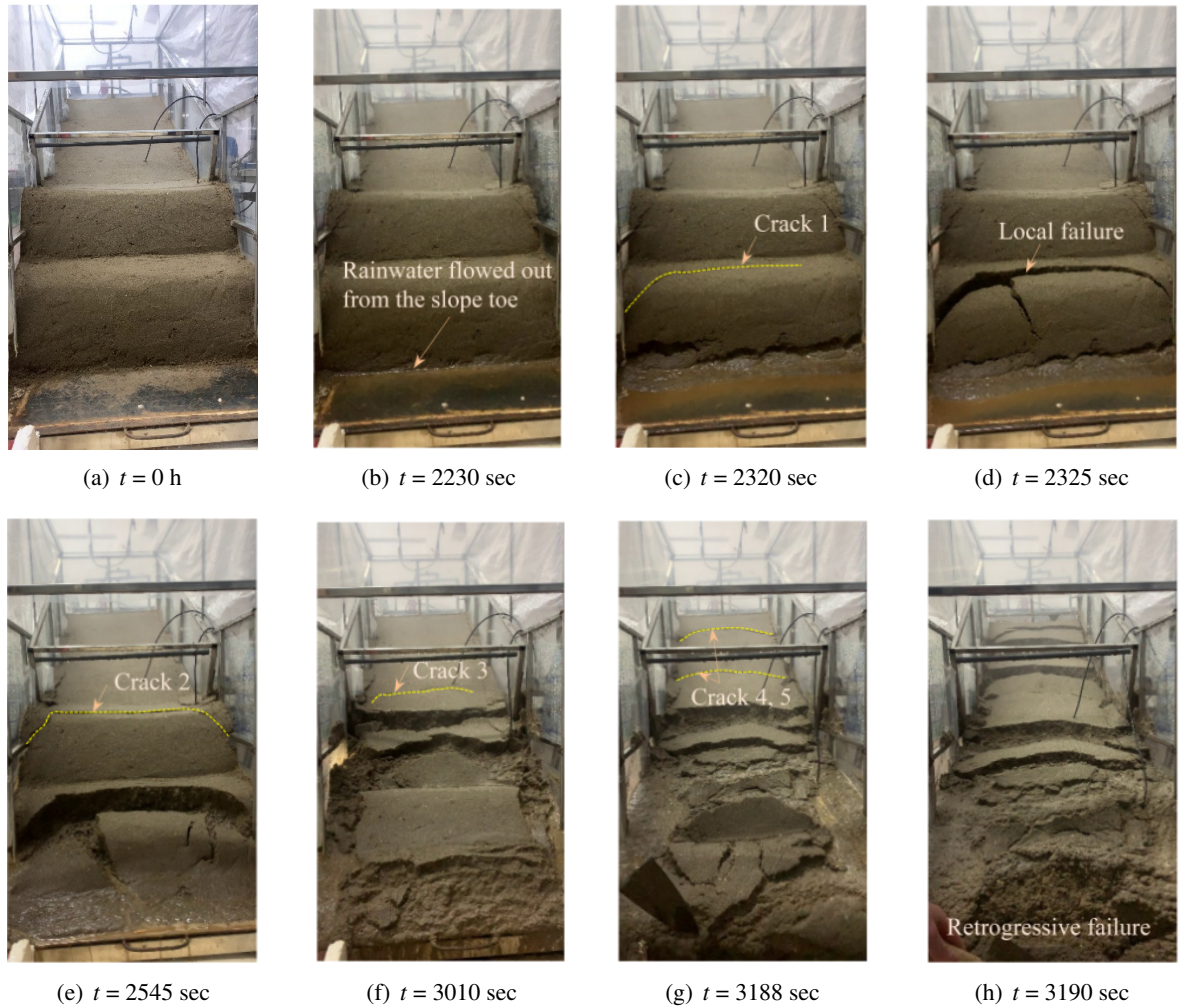| (e) $t = 2545$ sec | (f) $t = 3010$ sec | (g) $t = 3188$ sec | (h) $t = 3190$ sec |

Figure 7. Photograph of the failure process for slope at various times

Fig. 7 shows the failure process of the slope model taken by the video camera. The initial failure is determined by the appearance of tension cracks, soil erosion As shown in Fig. 7, rainwater began to flow out from the slope toe after about 2230 s (Fig. 7(b)) from the initiation of the rainfall as the seepage surface, indicating rainwater accumulated and positive PWP began to develop at the soil–base interface. Cracks primarily appeared at the front edge of the slope and the deformation started near the toe with the water table rising at $t_{cr} = 2320$ s (Fig. 7(c)). The experimental result indicates that

the toe of the slope is slightly washed away by the seepage erosion at the toe of the slope. A local slip failure in the form of small rotational slide in the slope toe with a long crack across the then appeared at $t = 2325$ s after the beginning of rainfall (Fig. 7(d)). As the rainfall continued, the range of failure gradually spread to the top of the slope with the appearance of the new cracks (Fig. 7(e), (f), (g)) which caused a rapid increase of the saturation in the lower part of the slope due to providing a preferential flow channels for water movement; and eventually the retrogressive development to the top of the slope and total slope failure occurred at $t_f = 3190$ s with an uppermost scarp approximately parallel to the line of the slope toe (Fig. 7(h)) Overall sliding failure occurred very quickly from $t = 3188$ s to 3190 s as deep-seated failures. The observed failure mode is similar to the experimental results reported by Chueasamat et al. [25], Wang et al. [30]. Notably, no runoff was observed in the test because the infiltration capacity of the sand layer was much higher than the rainfall intensities (i.e., $q/k_s = 0.1$). The surface sand slope was not yet reached saturation even if failure occurred Fig. 8 presents the captured aerial photography of the slope surface at various times of the experiment.

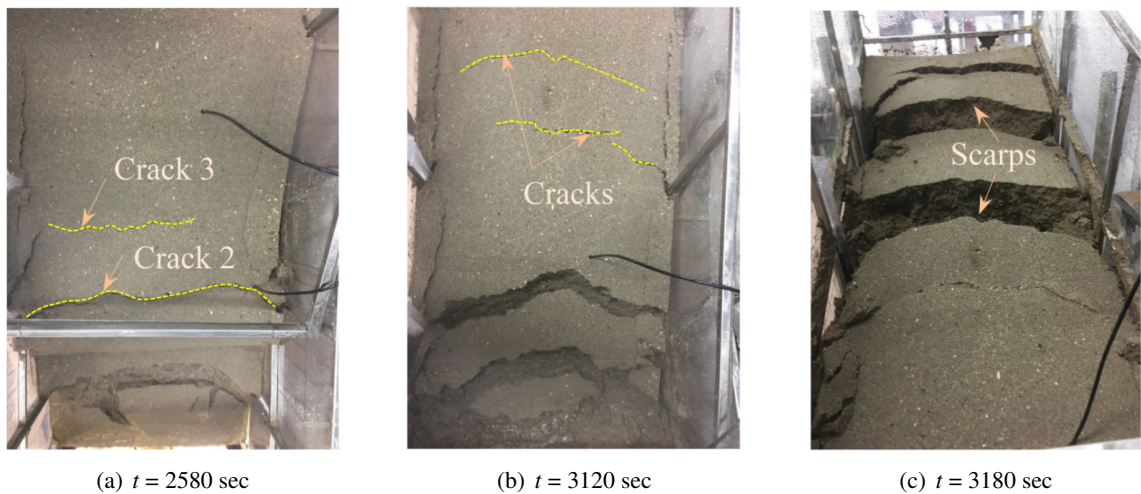| (a) $t = 2580$ sec | (b) $t = 3120$ sec | (c) $t = 3180$ sec |

Figure 8. Photograph of top views of the model at different times

Fig. 9 shows the measured soil moisture content at two monitoring positions in the slope model. It was observed that the initial moisture content obtained from sensor measurements before the initiation of rainfall exceeded the initial target value of 13.3%. Specifically, the moisture content at SM2 and SM1 sensors before the onset of rainfall was approximately 15.1% and 38.4%, respectively (Fig. 9). The nonuniform water content distribution in the model at the start of the test could be explained by the construction time of the model extends half a day and evaporation, hydraulic properties of the sand, and internal redistribution of water content took place simultaneously. The increase in soil moisture was observed with the advancement of the wetting front during the infiltration of the rainfall. As shown in Fig. 9, development of moisture content at MS2 over time shows a variation of four stages: the initial unsaturated stage without an obvious increase in moisture content until $t = 1080$ s, transition stage with a considerable increase in moisture content due to the impact of infiltration, from 15% to 29.9%, temporary equilibrium stage just prior to failure, and development stage up to slope failure due to rainwater accumulated and significant built up of positive PWP at the soil–bedrock interface. The slope starts to move after $t = 2220$ s, which corresponds to the time required for the wetting front to reach the base of the soil and the moisture content value of SM2 reached 37.5%. By combining the results shown in Figs. 7 and 8, it can be seen that large deformation as retrogressive failure mode

occurred at $t = 3188$ s when the soil moisture content at MS1 showed an abrupt increase from 48.3% to 100%, indicating that soil in the lower part of the slope reached a saturated state. The response of the sensors exhibited progressive seepage.
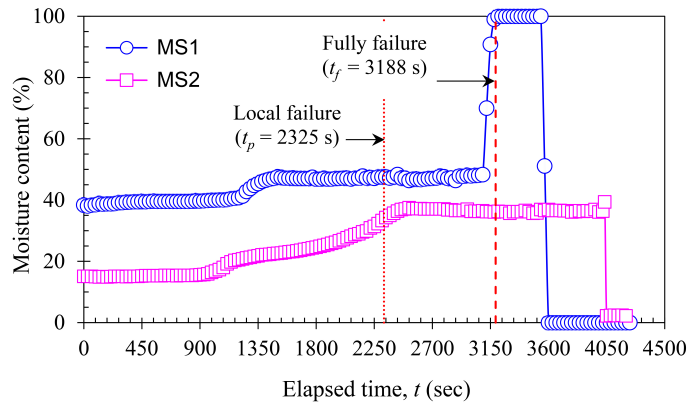

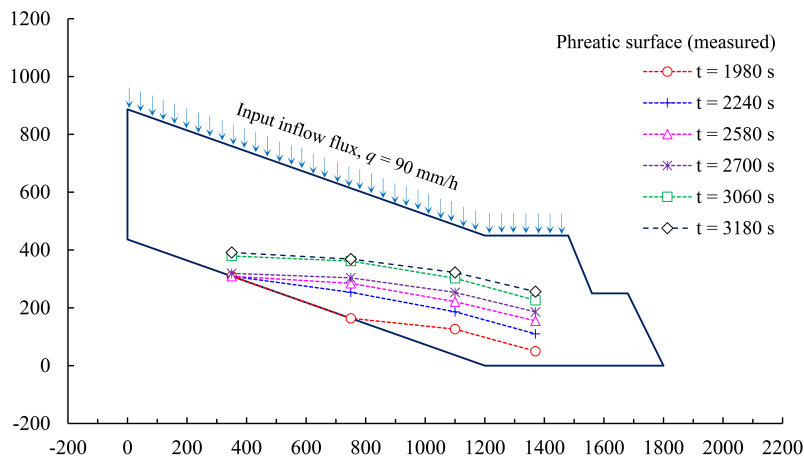Figure 9. Measured moisture contents during the test

Figure 10. Variation of phreatic levels with time in the flume experiment

Fig. 10 shows the evolution of the groundwater level recorded from the measuring manometer tubes at the 4 different locations along the slope from the time of rainfall initiation. As indicated in Fig. 10, the measurement results of the water level in tubes showed that the water level rises sooner in the lower measuring tube than in the upper measuring tubes. Based on the visual observations, manometer tubes response to the rainfall was registered after the rain had fallen for approximately 33 min at locations M3 and M4. Interestingly, the water table was not observed at M1 location by the time of local failure at the slope toe (i.e., $t = 2325$ s). The manometer tubes response showed that the upper part of the slope model had still maintained an unsaturated state. After about 2700 s (45 min) from the initiation of the rainfall, the observed water level elevation in tube M1 was about 1 cm, indicating that the accumulation of water at the slope base began to develop. Since then the rise in the water table continued quickly until total failure occurred.

4. Numerical Modeling

In this section, the numerical modeling using SEEP/W program [26] was applied to simulate the transient PWP conditions over time of unsaturated soil in the flume test Subsequently, the PWP conditions generated by SEEP/W were inputted into the SLOPE/W program [31] to perform stability analysis and determine the factor of safety (FS) values. The stability analysis was carried out utilizing limit equilibrium (LE) analysis (i.e., simplified Bishop's method) in which the failure surface is assumed to be circular The groundwater level, failure timing and location of the critical failure surface were compared with experimental results.

In the transient seepage analysis, the relationship between the change in water pressure head and change in volumetric water content can be expressed based on Richards [32] equation of transient unsaturated flow. This equation can be expressed in two-dimensional flow of water as follow:

$$\frac{\partial}{\partial x}\left(k_x \frac{\partial h}{\partial x}\right) + \frac{\partial}{\partial y}\left(k_y \frac{\partial h}{\partial y}\right) + q = \frac{\partial \theta_w}{\partial t} = m_w \gamma_w \frac{\partial h}{\partial t} \tag{2}$$

where h is total hydraulic head; k_x is unsaturated hydraulic conductivity in the xdirection; k_y is unsaturated hydraulic conductivity in the ydirection; m_w is coefficient of water volume change (slope of the water characteristics curve); γ_w is unit weight of water; q is applied unit flux; and θ_w is volumetric water content.

van Genuchten–Mualem's model [33] was used to describe the relationship between matric suction and volumetric water content, expressed as follows:

$$\Theta = \frac{\theta_w - \theta_r}{\theta_s - \theta_r} = \left[\frac{1}{1 + [\alpha(u_a - u_w)]^n}\right]^{1-1/n} \tag{3}$$

Additionally, the hydraulic conductivity function was proposed by Mualem [34] based on the soil-water characteristic curve and it can be described by the following formula:

$$k_{rel} = \frac{k_{(\Theta)}}{k_s} = \Theta^{1/2}\left[1 - \left(1 - \Theta^{1/(1-1/n)}\right)^{1-1/n}\right]^2 \tag{4}$$

where Θ is the normalized volumetric water content; θ_s is the saturated volumetric water content; θ_r is the residual volumetric water content; $(u_a - u_w)$ is the matric suction (where u_a and u_w are the pore-air and pore-water pressures, respectively); α and n are the curve fitting parameters in van Genuchten-Mualem's model [33]; k_{rel} is the relative hydraulic conductivity; k_{Θ} is the hydraulic conductivity at any soil degree of saturation; and k_s is the saturated hydraulic conductivity.

The unsaturated soil shear strength function proposed by Vanapalli et al. [35] was used in the slope stability analysis to determine FS:

$$\tau = c' + (\sigma_n - u_a)\tan\phi' + \Theta(u_a - u_w)\tan\phi' \tag{5}$$

where τ represents soil shear strength; c' is the effective cohesion; ϕ' is the effective friction angle; and σ_n is the total normal stress on the failure plane; $(\sigma_n - u_a)$ is the net normal stress (σ_n and u_a are the total normal stress and pore-air pressure acting on the failure plane, respectively).

In this study, the soil-water characteristic curve of non-plastic soils was first estimated based on the soil grain-size distribution and index properties [36]. Figs. 11 and 12 present the soil-water characteristic curve and hydraulic conductivity function of the soil test used for the numerical simulation. The soil properties and the initial conditions used in numerical simulation are summarized in Table 1.

The internal friction angle and cohesion of soil are 32.5° and 0.2 kPa, respectively used in the FE analysis were calibrated through a trial and error approach to match the experimental failure time and location of the critical failure surface The initial water content was approximately 16% by volume, equivalent to a soil suction of 5.4 kPa (Fig. 11).
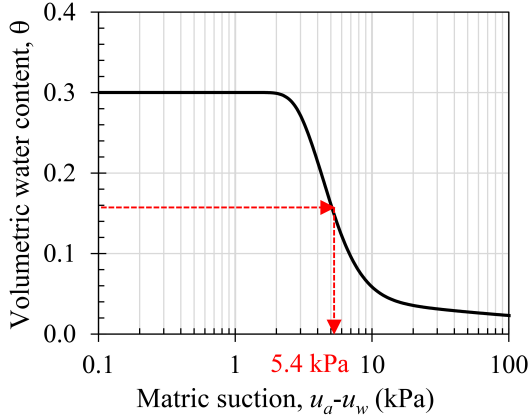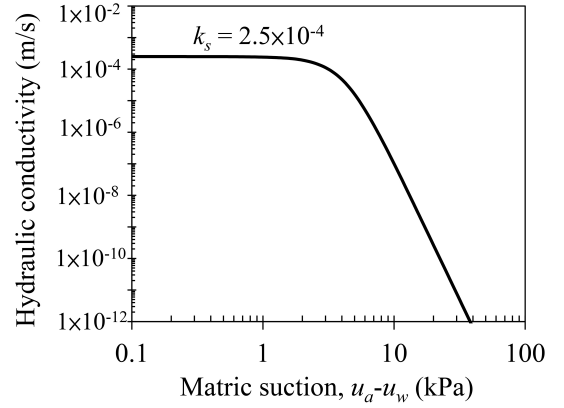
Figure 11. Soil-water characteristic curve

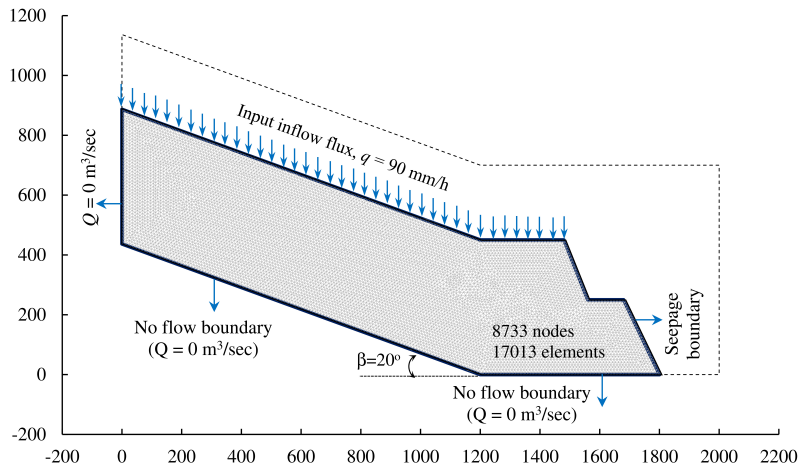Figure 12. Hydraulic conductivity function

Figure 13. Numerical model of the slope, mesh generation and boundary conditions

Fig. 13 shows the numerical model and hydraulic boundaries of the slope model. The finite element mesh consisted of 8733 nodes and 17013 triangular elements. Rainfall intensity of 90 mm/h was prescribed as inflow flux on the slope surfaces to simulate the artificial rainfall condition during the model test. A non-ponding boundary condition was specified on the slope surface to avoid excessive accumulation of rainfall. To allow seepage to flow out of the slope (i.e., free drainage surfaces), once PWP became positive at any node on the slope facing surfaces, the boundary condition was switched from the flux-specified boundary condition to a pressure-head-specified boundary condition (h_p = 0 m). The seepage boundary was defined at the right boundary of the model to enable variations in the phreatic level during the simulation of rainfall infiltration. A closed boundary (i.e., zero flux) was applied to the base of the model test, allowing the influence of the build-up of a positive PWP from the bottom of the slope to be examined. In this numerical analyses, the initial condition with a negative PWPs of 5.4 kPa was assigned on the entire slope.

4.1. Porewater pressure responses

Fig. 14 displays the variation of PWP contours and the development of phreatic level at different time intervals obtained from numerical analysis. The results revealed that PWP remained negavtive values before $t = 2220$ s. As rainfall proceeds, PWP increased and became slightly larger than zero at the slope base, indicative of the development of small positive PWPs and rainfall reached the base of the soil at $t = 2220$ s (37 min.) which is consistent with the result of experimental observation as indicated in Fig. 7(b) As the rainfall continued to infiltrate into the soil, rainwater accumulated and positive PWP began to rise at the soil–bedrock interface at the lower part of the slope. The slope failure was initiated in the lower part of the slope at $t = 2700$ s (corresponding FS = 0.929). As indicated in Fig.14(b), although the numerical simulation cannot capture the local failure at slope toe the simulated sliding failure surface closely matches that of visual observation at $t = 2700$ s (Fig. 8(b)). The PWP increased rapidly until 3180 s, reached a peak value of 2.5 kPa. Generally, the build-up of positive

(a) $t = 0$ sec

(b) $t = 2220$ sec

(c) $t = 2640$ sec

(d) $t = 2700$ sec

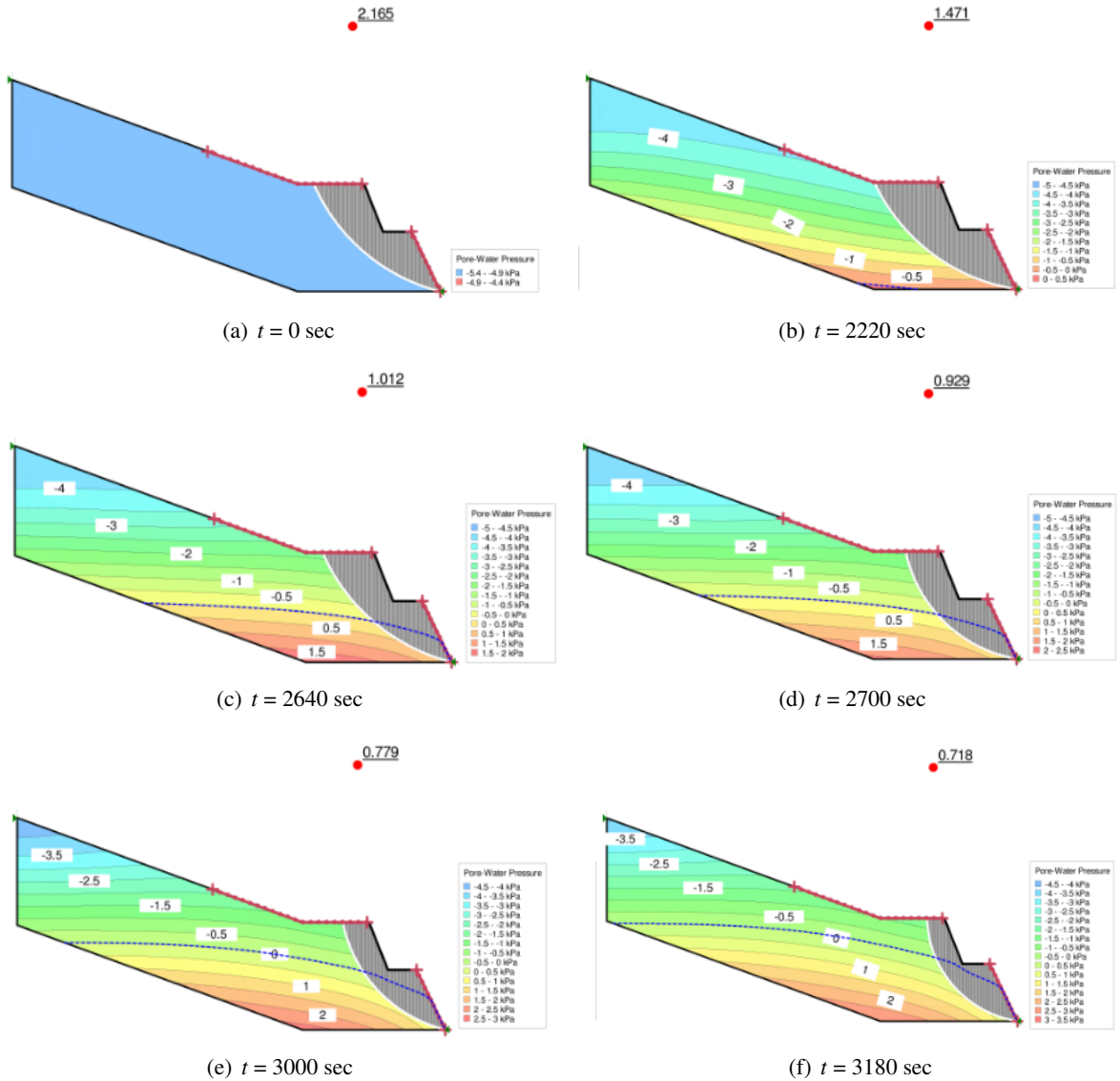(e) $t = 3000$ sec

(f) $t = 3180$ sec

Figure 14. Contours of simulated PWPs and slope stability level against rainfall time

PWPs and moisture content within the slope under rainfall conditions are the main factor causing slope failure. Fig. 14 also shows the predicted failure surface locations with the change in the suction profile due to rainfall infiltration. It was observed that the FS decreases rapidly with the increase of rainfall duration. At $t = 0$ s, the slope is in a stable state with FS value of 2.165 because of high initial matric suction. As the duration of rainfall increases, FS decreases continuously and FS of slope was closes to 1.0 at 2640 s after the rainfall started. The position of the potential sliding surface tends to pass through the toe of the slope. Unfortunately, limit equilibrium method using in SLOPE/W cannot describe the development of the slip surfaces because it involves large deformation problems.

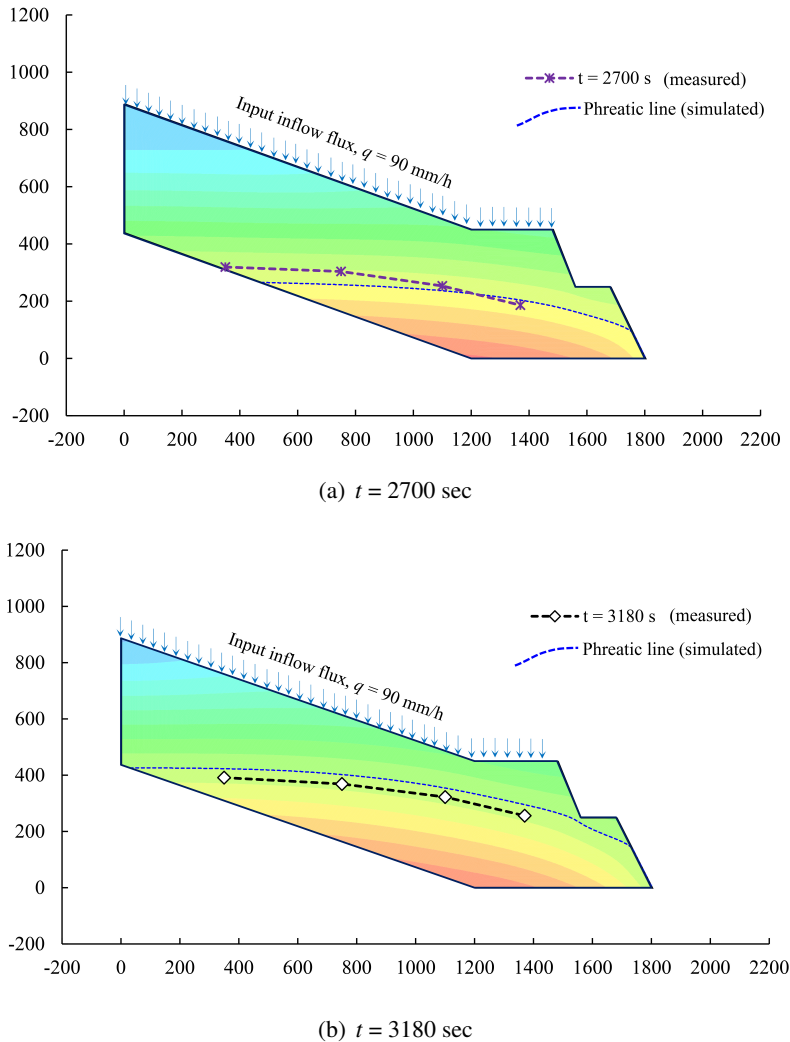(a) $t = 2700$ sec

(b) $t = 3180$ sec

Figure 15. Comparison of measured and calculated phreatic line (blue-dashed line) at each time step

A comparison on the phreatic line between experimental data and results from simulations is shown in Fig. 15. It was observed that the computed phreatic level obtained from the FEM simulation at $t = 2700$ s and 3180 s correlated well with the monitored results. At time $t = 2700$ s, the predicted phreatic surface was slightly lower than the measured value. This can be attributed to the initial suction distribution, which significantly influences the change in PWP during rainfall infiltration Achieving uniformity in the distribution of initial suction in the experimental model is often

challenging, resulting in higher values observed at the base of the slope model. However, by time $t = 3180$ s (i.e., when the slope had completely failed), the groundwater prediction exhibited an opposing trend, showing higher levels than those measured The main reason for this discrepancy was that the slope configuration in the experimental model was no longer maintained as originally intended (see Fig. 7(h)). Consequently, water rising within the slope could escape in various directions, causing the elevation of the water level in the observation manometer tubes to be notably lower than the simulated result.

5. Conclusions

In this study, a physical model test and numerical analysis were conducted to investigate hydraulic responses and failure mechanisms of slope under rainfall infiltration Measured values of the soil moisture and phreatic level were used to compare with the simulation results. The following conclusions can be drawn:

- The model test results revealed that the failures of the slope model the failures of the slope model primarily originated from the formation of an unstable area near the slope toe, manifesting as seepage erosion induced by water impoundment and subsequent buildup of water levels at the slope base. The onset of slope failure exhibited a direct correlation with the development of the phreatic line within the soil.

- Analysis of observed failure mechanisms indicated that the rise of the groundwater level instigated sliding at the slope toe, further leading to retrogressive sliding and cracking extending towards the slope's crest. The outcomes derived from the flume experiment showed a backward retrogressive failure pattern of the slope. Moreover, the emergence and propagation of cracks towards the upper regions of the slope were also identified as pivotal factors triggering deep-seated slope failure.

- A reasonable agreement between measured and simulated positions of phreatic level and failure surface was observed, demonstrating the numerical proposed is capable of quantitatively well the hydraulic responses of slopes subjected to rainfall infiltration.

The findings of this experiment provide valuable insights into the failure mechanisms of slopes induced by rainfall infiltration, underscoring the critical importance of preventing the formation of a phreatic surface within the slope, particularly through mitigating rainwater accumulation at the slope toes. However, the present study did not consider the influence of the rainfall intensity patterns and soil relative density on failure mode and failure mechanism of slope, nor did it address the influence of nonuniform soil moisture distribution in the numerical model. Furthermore, limitations persist in accurately observing and determining factors such as groundwater levels, depth of the failure surface, and deformation processes due to constraints related to measuring equipment. Hence, future experimental endeavors should prioritize the incorporation of advanced measurement techniques to more comprehensively investigate the evolutionary dynamics of slope failure triggered by rainfall infiltration.

References

[1] Petley, D. (2012). Global patterns of loss of life from landslides. *Geology*, 40(10):927–930.
[2] Segoni, S., Piciullo, L., Gariano, S. L. (2018). A review of the recent literature on rainfall thresholds for landslide occurrence. *Landslides*, 15(8):1483–1501.
[3] Froude, M. J., Petley, D. N. (2018). Global fatal landslide occurrence from 2004 to 2016. *Natural Hazards and Earth System Sciences*, 18(8):2161–2181.

[4] Guzzetti, F., Peruccacci, S., Rossi, M., Stark, C. P. (2007). The rainfall intensity–duration control of shallow landslides and debris flows: an update. *Landslides*, 5(1):3–17.

[5] Acharya, K. P., Bhandary, N. P., Dahal, R. K., Yatabe, R. (2014). Seepage and slope stability modelling of rainfall-induced slope failures in topographic hollows. *Geomatics, Natural Hazards and Risk*, 7(2): 721–746.

[6] Harrison, J. F., Chang, C.-H. (2019). Sustainable Management of a Mountain Community Vulnerable to Geohazards: A Case Study of Maolin District, Taiwan. *Sustainability*, 11(15):4107.

[7] Collins, B. D., Znidarcic, D. (2004). Stability analyses of rainfall induced landslides. *Journal of geotechnical and geoenvironmental engineering*, 130(4):362–372.

[8] Moriwaki, H., Inokuchi, T., Hattanji, T., Sassa, K., Ochiai, H., Wang, G. (2004). Failure processes in a full-scale landslide experiment using a rainfall simulator. *Landslides*, 1(4):277–288.

[9] Cogan, J., Gratchev, I. (2019). A study on the effect of rainfall and slope characteristics on landslide initiation by means of flume tests. *Landslides*, 16(12):2369–2379.

[10] Wang, G., Sassa, K. (2001). Factors affecting rainfall-induced flowslides in laboratory flume tests. *Géotechnique*, 51(7):587–599.

[11] Lee, K., Suk, J., Kim, H., Jeong, S. (2020). Modeling of rainfall-induced landslides using a full-scale flume test. *Landslides*, 18(3):1153–1162.

[12] Ng, C. W. W., Zhan, L. T., Bao, C. G., Fredlund, D. G., Gong, B. W. (2003). Performance of an unsaturated expansive soil slope subjected to artificial rainfall infiltration. *Géotechnique*, 53(2):143–157.

[13] Yang, K.-H., Nguyen, T. S., Rahardjo, H., Lin, D.-G. (2020). Deformation characteristics of unstable shallow slopes triggered by rainfall infiltration. *Bulletin of Engineering Geology and the Environment*, 80(1):317–344.

[14] Yang, K.-H., Uzuoka, R., Thuo, J. N., Lin, G.-L., Nakai, Y. (2017). Coupled hydro-mechanical analysis of two unstable unsaturated slopes subject to rainfall infiltration. *Engineering Geology*, 216:13–30.

[15] Tran, T. V., Alvioli, M., Hoang, V. H. (2021). Description of a complex, rainfall-induced landslide within a multi-stage three-dimensional model. *Natural Hazards*, 110(3):1953–1968.

[16] Lumb, P. (1962). Effect of rain storms on slope stability. In *Symposium on Hong Kong Soils, Hong Kong*, 73–87.

[17] Heber Green, W., Ampt, G. A. (1911). Studies on Soil Phyics. *The Journal of Agricultural Science*, 4(1): 1–24.

[18] Thang, N. V., Wakai, A., Sato, G., Viet, T. T., Kitamura, N. (2022). Simple method for shallow landslide prediction based on wide-area terrain analysis incorporated with surface and subsurface flows. *Natural Hazards Review*, 23(4):04022028.

[19] Iverson, R. M. (2000). Landslide triggering by rain infiltration. *Water Resources Research*, 36(7):1897–1910.

[20] Wang, F., Shibata, H. (2007). Influence of soil permeability on rainfall-induced flowslides in laboratory flume tests. *Canadian Geotechnical Journal*, 44(9):1128–1136.

[21] Wang, G., Sassa, K. (2003). Pore-pressure generation and movement of rainfall-induced landslides: effects of grain size and fine-particle content. *Engineering Geology*, 69(1–2):109–125.

[22] Tohari, A., Nishigaki, M., Komatsu, M. (2007). Laboratory rainfall-induced slope failure with moisture content measurement. *Journal of Geotechnical and Geoenvironmental Engineering*, 133(5):575–587.

[23] Schnellmann, R., Busslinger, M., Schneider, H. R., Rahardjo, H. (2010). Effect of rising water table in an unsaturated slope. *Engineering Geology*, 114(1–2):71–83.

[24] Regmi, R. K., Jung, K., Nakagawa, H., Kang, J. (2014). Study on mechanism of retrogressive slope failure using artificial rainfall. *CATENA*, 122:27–41.

[25] Chueasamat, A., Hori, T., Saito, H., Sato, T., Kohgo, Y. (2018). Experimental tests of slope failure due to rainfalls using 1g physical slope models. *Soils and Foundations*, 58(2):290–305.

[26] Geo-Slope International Ltd (2012). *Seep/W for finite element seepage analysis: user's guide*. GEO-SLOPE International Ltd, Calgary, Alberta, Canada.

[27] Mhaske, S. N., Pathak, K., Basak, A. (2019). A comprehensive design of rainfall simulator for the assessment of soil erosion in the laboratory. *CATENA*, 172:408–420.

[28] Christiansen, J. E. (1941). The uniformity of application of water by sprinkler systems. *Agricultural Engineering*, 22(3):89–92.

[29] Aksoy, H., Unal, N. E., Cokgor, S., Gedikli, A., Yoon, J., Koca, K., Inci, S. B., Eris, E. (2012). A rainfall simulator for laboratory-scale assessment of rainfall-runoff-sediment transport processes over a two-dimensional flume. *Catena*, 98:63–72.

[30] Wang, S., Idinger, G., Wu, W. (2021). Centrifuge modelling of rainfall-induced slope failure in variably saturated soil. *Acta Geotechnica*, 16(9):2899–2916.

[31] Geo-Slope International Ltd (2012). *Slope/W for slope stability analysis: user's guide*. GEO-SLOPE International Ltd, Calgary, Alberta, Canada.

[32] Richards, L. A. (1931). Capillary conduction of liquids through porous mediums. *Physics*, 1(5):318–333.

[33] van Genuchten, M. T. (1980). A Closed-form Equation for Predicting the Hydraulic Conductivity of Unsaturated Soils. *Soil Science Society of America Journal*, 44(5):892–898.

[34] Mualem, Y. (1976). A new model for predicting the hydraulic conductivity of unsaturated porous media. *Water Resources Research*, 12(3):513–522.

[35] Vanapalli, S. K., Fredlund, D. G., Pufahl, D. E., Clifton, A. W. (1996). Model for the prediction of shear strength with respect to soil suction. *Canadian Geotechnical Journal*, 33(3):379–392.

[36] Fredlund, D. G., Xing, A. (1994). Equations for the soil-water characteristic curve. *Canadian Geotechnical Journal*, 31(4):521–532.